



Thermal instability in a ferrimagnetic resonator strongly coupled to a loop-gap microwave cavity

Cijy Mathai , Oleg Shtempluck, and Eyal Buks 

Andrew and Erna Viterbi Department of Electrical Engineering, Technion, Haifa 32000, Israel



(Received 2 May 2021; revised 19 July 2021; accepted 9 August 2021; published 20 August 2021)

We study the nonlinear response of a ferrimagnetic sphere resonator (FSR) strongly coupled to a microwave loop-gap resonator (LGR). The measured response in the regime of weak nonlinearity allows the extraction of the FSR Kerr coefficient and its cubic damping rate. We find that there is a certain range of driving parameters in which the system exhibits instability. In that range, self-sustained modulation of the reflected power off the system is generated. The instability is attributed to absorption-induced heating of the FSR above its Curie temperature.

DOI: [10.1103/PhysRevB.104.054428](https://doi.org/10.1103/PhysRevB.104.054428)

I. INTRODUCTION

Ferromagnetic and ferrimagnetic resonators [1–3] are widely employed in a variety of microwave (MW) devices, including narrow-band oscillators [4], filters [5], and parametric amplifiers [6]. These resonators exhibit a variety of intriguing physical effects [7], including Bose-Einstein condensation [8] and magneto-optical coupling [9–12]. Here, we study a strongly coupled hybrid system composed of a loop-gap resonator (LGR) integrated with a ferrimagnetic sphere resonator (FSR) made of yttrium iron garnet (YIG) [13,14]. We focus on the regime of nonlinear response. In Sec. III below we explore the effect on nonlinear damping in the region of relatively weak microwave driving. An instability, which is observed with a much stronger driving, is reported in Sec. IV below, and a theoretical model, which attributes the instability to a driving-induced heating, is presented.

Many nonlinear dynamical effects have been observed before in FSRs, including auto-oscillations [15,16], optical cooling [17], frequency mixing [18,19], and bistability [20–24]. The Suhl instability (of both first and second orders) has been observed with transverse microwave driving, whereas parallel pumping instability has been observed with longitudinal driving [25]. Applications of nonlinearity for quantum data processing have been explored in Refs. [26–33].

Heating a YIG sphere from room temperature to 400 K by microwave driving having a power of 450 mW has been reported in Ref. [34]. At a Curie temperature given by $T_c = 560$ K, YIG undergoes a phase transition between an ordered ferrimagnetic state (FS) and a disordered paramagnetic state (PS). Thermal instability was observed in a cavity magnetomechanical system [35]. Microwave oscillations induced by injecting spin-polarized current [36] into a magnetic-multilayer structure have been reported in Ref. [37]. Self-excited oscillations induced by ohmic heating in a $Y_3Fe_5O_{12}/Pt$ bilayer nanowire have been investigated in Ref. [38]. Imaging of heating induced by the spin Peltier effect has been demonstrated in Ref. [39].

II. LOOP-GAP RESONATOR

With relatively low input power, the main mechanisms responsible for the FSR nonlinear response are magnetic anisotropy [40] and an exchange interaction [13]. Consider a MW cavity mode having angular frequency ω_e and an integrated FSR having radius R_s . It is assumed that the applied static magnetic field \mathbf{H}_s is parallel to the easy axis. In the Holstein-Primakoff approximation [41] (which assumes that magnetization is nearly saturated), the Hamiltonian of the system \mathcal{H}_D is expressed as [21,42]

$$\begin{aligned} \hbar^{-1}\mathcal{H}_D = & \omega_e N_e + \omega_s N_s + K_M N_s^2 \\ & + g_{\text{eff}}(A_e^\dagger A_s + A_e A_s^\dagger), \end{aligned} \quad (1)$$

where $N_e = A_e^\dagger A_e$ ($N_s = A_s^\dagger A_s$) is a cavity mode (FSR Kittel mode) number operator, $\omega_s = \gamma_g H_s$ is the Kittel mode angular frequency, $\gamma_g/2\pi = 27.98$ GHz T⁻¹ is the gyromagnetic ratio, $K_M = \hbar\gamma_g^2 K_{c1}/(V_s M_s^2)$ is the anisotropy-induced Kerr frequency, K_{c1} is the first-order anisotropy constant, $V_s = 4\pi R_s^3/3$ is the volume of the sphere, M_s is the saturation magnetization, and g_{eff} is the cavity-FSR coupling coefficient. For YIG at room temperature, $M_s = 140$ kA/m and $K_{c1} = -610$ J/m³, hence $K_M = -2.4 \times 10^{-8}$ Hz $\times [R_s/(100 \mu\text{m})]^{-3}$.

In the linear regime, where the Kerr nonlinearity can be disregarded, the Hamiltonian \mathcal{H}_D (1) can be diagonalized. The angular frequencies ω_\pm of the two hybrid photon-magnon eigenmodes are given by [43]

$$\omega_\pm = \frac{\omega_e + \omega_s}{2} \pm \sqrt{\left(\frac{\omega_e - \omega_s}{2}\right)^2 + g_{\text{eff}}^2}. \quad (2)$$

Both angular frequencies ω_\pm are positive provided that $g_{\text{eff}} < \sqrt{\omega_s \omega_e}$. Note that the superradiance Dicke instability occurs in the ultrastrong coupling region where $g_{\text{eff}} > \sqrt{\omega_s \omega_e}$ [44]. In the rotating wave approximation (RWA) the Kerr coefficients K_\pm of the hybrid modes having angular frequencies ω_\pm are given by Eqs. (A9) and (A10) of the Appendix [see Eq. (A8)].

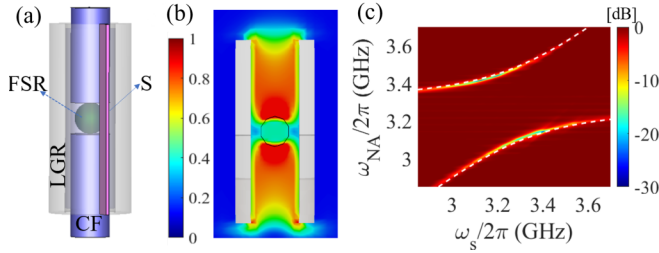


FIG. 1. FSR-LGR coupling: (a) A sketch of the FSR made of YIG having a radius of $R_s = 1$ mm that is integrated inside the aluminum cylindrical LGR having a gap width of 0.3 mm. The sphere is held by ceramic ferrules (CFs). A sapphire wafer (labeled as S) is inserted into the gap to increase the capacitance. (b) The numerically calculated magnetic field energy density distribution (normalized with respect to the maximum value) corresponding to driving at the resonance frequency $\omega_e/(2\pi) = 3.3$ GHz. (c) A VNA reflectivity $|S_{11}|^2$ measurement as a function of magnon frequency ω_s (proportional to the externally applied magnetic field). The coupling coefficient g_{eff} is extracted from the theoretical fit (white dashed lines) following Eq. (2).

In the current experiment, we explore the response for a wide range of MW input powers P_p . We find that the response is well described by the Hamiltonian \mathcal{H}_D provided that P_p is sufficiently small. However, with sufficiently high P_p , the FSR temperature T may exceed the Curie temperature T_c due to MW absorption-induced heating. We study the response of the FSR-LGR system to an injected monochromatic pump tone having a frequency close to resonance. The off-reflected power is measured using a spectrum analyzer (SA). We find that there is a certain zone in the pump frequency–pump amplitude plane, in which the resonator exhibits a limit-cycle (LC) response resulting in self-sustained modulation of the reflected power. The observed LC is attributed to thermal instability (TI) [45].

A MW cavity made of an LGR allows achieving a relatively large coupling coefficient g_{eff} [46,47]. The MW LGR, schematically shown in Fig. 1(a), is made of a hollow concentric aluminum tube having an inner and outer radii of $R_{\text{LGR}} = 1.7$ and 3 mm, respectively, and a height of $H_{\text{LGR}} = 12$ mm. A sapphire strip of 260 μm thickness has been inserted into the gap in order to increase its capacitance, which in turn reduces the frequency f_e of the LGR fundamental mode [$f_e = \omega_e/(2\pi) = 3.3$ GHz with sapphire] [48]. An FSR made of YIG having a radius of $R_s = 1$ mm is held by two ferrules inside the LGR. The static magnetic field \mathbf{H}_s is applied perpendicularly to the LGR axis. The LGR-FSR coupled system has been encapsulated in a metallic rectangular shield made of aluminum. The cavity is weakly coupled to a loop antenna (LA).

The numerically calculated magnetic energy density distribution corresponding to the LGR fundamental mode is shown in Fig. 1(b). The calculated density is homogeneous ($\approx 95\%$) over the FSR volume, and it is well confined inside the LGR inner volume. Note that for our device, the LGR inner volume, which is given by $\pi R_{\text{LGR}}^2 H_{\text{LGR}}$, is four orders of magnitude smaller than the volume λ_e^3 , where $\lambda_e = c/f_e$ is the free-space wavelength corresponding to the LGR frequency f_e , and c

is the speed of light in vacuum. Consequently, the coupling coefficient g_{eff} can be made much larger than typical values obtained with the commonly employed rectangular cavities [28], for which the mode volume commonly has the same order of magnitude as λ_e^3 .

Based on Eq. (2) of Ref. [28], together with the evaluated energy density shown in Fig. 1(b), the calculated value of the coupling coefficient is found to be $g_{\text{eff}} = 176$ MHz for the LGR fundamental mode of frequency $f_e = 3.3$ GHz. Alternatively, g_{eff} can be extracted from measurements of the MW reflection coefficient $|S_{11}|^2$ as a function of the Kittel mode frequency $\omega_s/(2\pi)$ and driving frequency $\omega_{\text{NA}}/(2\pi)$. Fitting $|S_{11}|^2$, which is measured at a temperature of 3 K using a vector network analyzer (VNA), with Eq. (2) [see Fig. 1(c)] yields the value $g_{\text{eff}} = 200$ MHz, which is fairly close to the value obtained from simulation. Note that g_{eff} is only one order of magnitude smaller than the threshold value corresponding to the superradiance Dicke instability [44].

III. KERR COEFFICIENT AND NONLINEAR DAMPING

Cavity driving having an amplitude Ω_p and angular frequency ω_p is taken into account by adding a term given by $\hbar\Omega_p(A_e^\dagger e^{-i\omega_p t} + A_e e^{-i\omega_p t})$ to the Hamiltonian \mathcal{H}_D (1). The steady state solution of the driven system was calculated in Ref. [40] for the case where damping is taken into account to first order only. For that case the solution is found by solving a cubic equation for the FSR dimensionless energy $E_s = \langle N_s \rangle$ [given by Eq. (36) of Ref. [40]]. We find, however, that the calculated steady state yields only a moderate agreement with experimental data. Better agreement can be obtained by taking into account nonlinear damping to cubic order [49]. In this approach the cubic equation for E_s becomes

$$(\delta_s'^2 + \gamma_s'^2)E_s = \eta|\Omega_p|^2, \quad (3)$$

where $\delta_s' = \delta_s - \eta\delta_e + 2K_M E_s$, $\delta_s = \omega_s - \omega_p$, and $\delta_e = \omega_e - \omega_p$ are driving detuning angular frequencies, $\eta = g_{\text{eff}}^2/(\delta_e^2 + \gamma_e^2)$, $\gamma_e = \gamma_{1e} + \gamma_{2e}$ with γ_{1e} (γ_{2e}) being the external (intrinsic) cavity damping rate, $\gamma_s' = \gamma_s + \eta\gamma_e + \gamma_{3s}E_s$, γ_s is the FSR linear damping rate, and γ_{3s} is the FSR cubic nonlinear damping coefficient. Note that $|\Omega_p|^2$ is proportional to the driving power P_p injected into the LA. Note also that when nonlinear damping is disregarded (i.e., when $\gamma_{3s} = 0$), Eq. (3) becomes identical to Eq. (36) of Ref. [40].

VNA measurements of the reflection coefficient $|S_{11}|^2$ for three different values of P_p are shown in Figs. 2(a)–2(c). For the data presented in both Figs. 2 and 3, the radius of the FSR is $R_s = 0.1$ mm. The theoretical fit shown in Figs. 2(d)–2(f) is based on the cubic equation (3), which allows the calculation of the dimensionless energy E_s , and on Eq. (3) of Ref. [28], which evaluates the reflection coefficient $|S_{11}|^2$ as a function of E_s . The values of the parameters assumed for the calculations are listed in the caption of Fig. 2. Note the driving-induced blueshift observed in the magnetic resonance frequency [see Figs. 2(a)–2(c)]. This shift cannot be accurately reproduced theoretically when nonlinear damping is disregarded.

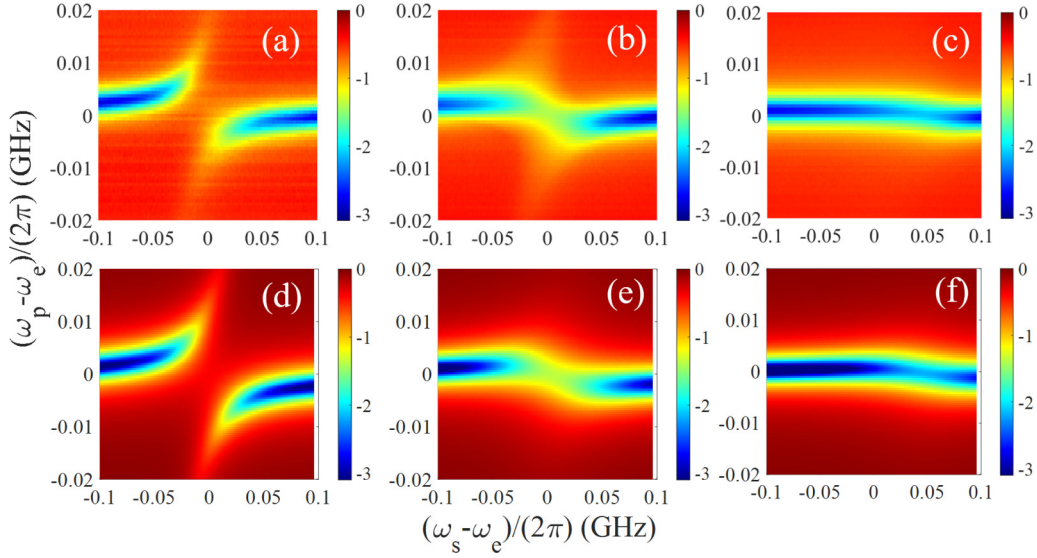


FIG. 2. Reflection coefficient $|S_{11}|^2$ in dB units for three values of MW input power P_p . (a)–(c) present the experimental data corresponding to MW input powers P_p of -20 , -5 , and $+10$ dBm, respectively. The second row [(d)–(f)] shows the corresponding theoretical fits that are obtained from Eq. (3). The theoretical fit parameters are $\gamma_{2e} = 1.5$ MHz, $\gamma_e = 4$ MHz, $\gamma_s = 1$ MHz, $K_M = 6.325$ nHz, $\delta_e = 35$ MHz, and $\gamma_{3s} = 0.001$ nHz. To obtain a proper fit, N_s and g_{eff} are taken as variable values varying as a function of P_p . For $P_p = -20$, -5 , and 10 dBm, N_s values are taken as 1×10^{19} , 5×10^{19} , and $8 \times 10^{19} \text{ m}^{-3}$, and g_{eff} values are taken as 14 , 14 , and 12 MHz, respectively.

IV. THERMAL INSTABILITY

Further insight can be gained by measuring the spectral density I_{SA} of the signal reflected off the LA using a SA (see Fig. 3). We find that for $P_p > P_c = 42.5$ dBm, and for sufficiently small detuning from resonance, the measured spectral density I_{SA} contains equally spaced sidebands (SBs) on both sides of the driving frequency $f_p = \omega_p/(2\pi)$ [see Fig. 3(a)]. We measure the SB spacing frequency $\omega_{SM}/(2\pi)$ as a function of the driving frequency f_p and driving power P_p [see Fig. 3(c)].

The observed equally spaced SBs are attributed to a thermal instability mechanism that is discussed in Ref. [45]. The phase transition occurring at the Curie temperature T_c between the FS and the PS gives rise to a sharp change in the resonance modes of the hybrid cavity-FSR system. Consider the case where the frequency of the externally applied driving is tuned very close to the frequency of one of the hybrid system modes. With a sufficiently high driving amplitude the temperature T of the FSR may exceed the Curie temperature T_c due to driving-induced heating. For that case no steady state with $T < T_c$ (i.e., FS) exists. The transition from the FS to the PS occurring at T_c is expected to give rise to a resonance frequency shift. Consequently, the driving-induced heating is expected to abruptly drop down, since above T_c the frequency detuning between the continuous wave external driving and the resonance frequency becomes larger (in absolute value). Consider the case where the reduced heating gives rise to a temperature drop below $T < T_c$. For this case, a steady state with $T > T_c$ (i.e., PS) also becomes impossible. In the region where no steady state is possible, the temperature is expected to oscillate around T_c . The frequency of temperature oscillation can be determined from the spacing between the measured SBs.

For the measurements presented in Fig. 3, the driving angular frequency ω_p is tuned close to ω_+ . The analysis is greatly simplified by disregarding the other hybrid eigenmode having an angular frequency ω_- . This approximation is applicable in the strong coupling regime, for which the resonances having angular frequencies ω_{\pm} do not overlap [see Eq. (2)]. In this approach the FSR-cavity system is treated as a single mode having an angular frequency $\omega_+ = 2\pi \times 3.32$ GHz, and Kerr coefficient $K_+ = K_M \sin^4(\theta_g/2)$ [see Eq. (A9)]. The mode damping rate $\gamma_+ = 30$ MHz is expressed as $\gamma_+ = \gamma_{1+} + \gamma_{2+}$, where γ_{1+} is the coupling coefficient between the driven mode and the LA, and γ_{2+} is the mode intrinsic damping rate (note that $\gamma_{1+} = \gamma_{2+}$ for critical coupling).

To account for the observed SB, we consider the effect of driving-induced heating on the FSR magnetic ordering. The externally applied driving gives rise to a heating power Q given by $Q = 2\hbar\omega_+\gamma_{2+}|B|^2$, where B is the complex amplitude of the driven mode (note that nonlinear damping is disregarded here). It is assumed that the FSR temperature T is uniform, and that the cooling power due to the coupling between the FSR and its environment at a base temperature of T_0 is given by $H(T - T_0)$, where H is the heat transfer coefficient. The thermal heat capacity of the FSR is denoted by C . It is assumed that all the parameters characterizing the mode abruptly change at a critical temperature given by T_c . In the adiabatic (diabatic) region, the mode linear damping rate γ_+ is much smaller (larger) than the thermal decay rate H/C .

In dimensionless form, the system's time evolution is governed by [45]

$$\dot{B} = wB - w_1, \quad (4)$$

$$\dot{\Theta} = \sigma|B|^2 - w_T\Theta. \quad (5)$$

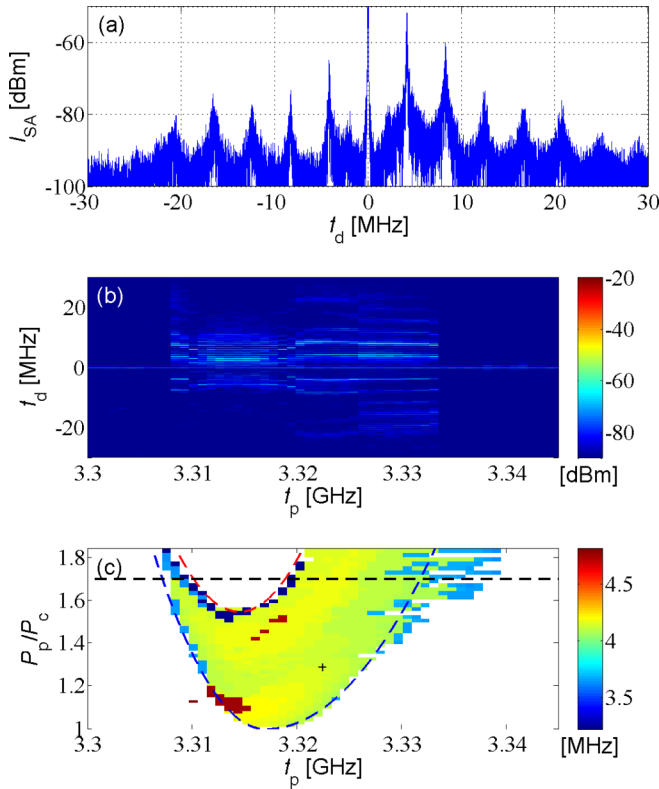


FIG. 3. Thermal instability. (a) Spectral density I_{SA} of the signal reflected off the LA, as a function of the detuning frequency f_d , for the driving frequency $f_p = 3.2224$ GHz and normalized driving power $P_p/P_c = 1.288$ specified by the black cross overlaid in (c). (b) Spectral density I_{SA} in dB as a function of the driving frequency f_p and detuning frequency f_d for $P_p/P_c = 1.7$ [indicated by the overlaid horizontal dashed line in (c)]. (c) The SB spacing frequency $\omega_{SM}/(2\pi)$ in MHz as a function of driving frequency f_p and normalized driving power P_p/P_c . The overlaid blue (red) dashed line represents the threshold condition $E_F = E_{cF}$ ($E_p = E_{cP}$). The following values are assumed for the calculations: $\omega_{+F}/2\pi = 3.317$ GHz, $\omega_{+P}/2\pi = 3.314$ GHz, $\gamma_{+F} = 1.3 \times \gamma_{+P}$, $\sigma_F/w_{TF} = 2.6 \times \sigma_P/w_{TP}$, $(K_{+F}/\gamma_{+F})(w_{TF}/\sigma_F) = 0.5$, and $K_{+P} = 0$.

The overdot denotes a derivative with respect to a dimensionless time τ , which is related to the time t by $\tau = \gamma_0 t$, where γ_0 is a constant rate. The dimensionless complex frequency w is given by $w = [i(\omega_p - \omega_+ - K_+|B|^2) - \gamma_+]/\gamma_0$, the dimensionless driving amplitude w_1 is given by $w_1 = i\gamma_0^{-1}\sqrt{2}\gamma_{1+}\Omega_p$, the dimensionless temperature Θ is given by $\Theta = (T - T_0)/(T_c - T_0)$, the dimensionless heating coefficient σ is given by $\sigma = 2\hbar\omega_+\gamma_{2+}\gamma_0^{-1}C^{-1}(T_c - T_0)^{-1}$, and the dimensionless thermal rate w_T is given by $w_T = (H/C)/\gamma_0$.

The normalized parameters w , w_1 , σ , and w_T are assumed to have a step function dependence on the temperature. Below (above) the critical temperature T_c , i.e., for $\Theta < 1$ ($\Theta > 1$), they take the values w_F , w_{1F} , σ_F , and w_{TF} (w_P , w_{1P} , σ_P , and w_{TP}), respectively. A steady state (i.e., time-independent) solution below (above) the critical temperature T_c , i.e., in the region $\Theta < 1$ ($\Theta > 1$), is possible provided that $E_F < E_{cF}$ ($E_p > E_{cP}$), where $E_F = |w_{1F}/w_F|^2$ and $E_{cF} = w_{TF}/\sigma_F$ ($E_p = |w_{1P}/w_P|^2$ and $E_{cP} = w_{TP}/\sigma_P$) [see Eqs. (4) and (5) and Fig. 4(b)]. Note that both E_F and E_p represent steady state

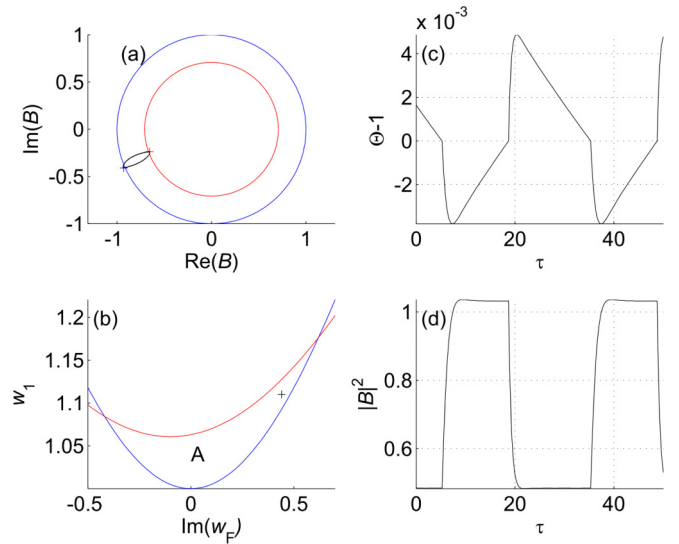


FIG. 4. Limit cycle. (a) Numerical integration of the equations of motion (4) and (5) is performed with the following parameters: $\text{Im}(w_F - w_P) = -0.1$, $\text{Re}(w_F) = -1$, $\text{Re}(w_P) = -1.5$, $\sigma_F = 0.01$, $\sigma_P = 0.02$, and $w_{TF} = w_{TP} = 0.01$. The values of driving detuning frequency $\text{Im}(w_F)$ and driving amplitude $w_1 = w_{1F} = w_{1P}$ are indicated by the black cross in (b). The LC is shown in (a) as a closed curve in the complex B plane, in (c) as a periodic function of $\Theta - 1$ vs the normalized time τ , and in (d) as a periodic function $|B|^2$ vs τ . The plane of driving frequency and driving amplitude is shown in (b). No steady state solution exists in the region between the blue and red curves (labeled as A).

values of Eq. (4) for $|B|^2$, whereas both E_{cF} and E_{cP} represent values of $|B|^2$, for which $\Theta = 1$ is a steady state value of Eq. (5).

Heat can be removed from the FSR by radiation, exchange with the surrounding air, and exchange with the supporting ferrules, which hold the FSR inside the LGR. The contributions to the total heat transfer coefficient H due to radiation, air, and the ferrules are denoted by $h_{\text{rad}}S_s$, $h_{\text{air}}S_s$, and H_{fer} , respectively, where $S_s = 4\pi R_s^2$ is the FSR surface area. The coefficient h_{rad} is roughly given by $h_{\text{rad}} \simeq \alpha_{\text{YIG}}\sigma_{\text{SB}}(T_c^4 - T_0^4)/(T_c - T_0)$, where α_{YIG} is the averaged FSR absorption coefficient in the spectral band corresponding to room-temperature $T_0 \simeq 300$ K radiation (wavelength $\lambda \simeq 10$ μm), $\sigma_{\text{SB}} = \pi^2 k_B^4/(60\hbar^3 c^2)$ is the Stefan-Boltzmann constant, k_B is the Boltzmann's constant, \hbar is Planck's constant, and $T_c = 560$ K is the YIG Curie temperature. The absorption coefficient value $\alpha_{\text{YIG}} \simeq 10^{-1}$ [50] yields $h_{\text{rad}} \simeq 2$ $\text{W m}^{-2} \text{K}^{-1}$. For ambient temperature and pressure $h_{\text{air}} \simeq 15$ $\text{W m}^{-2} \text{K}^{-1}$, hence $(h_{\text{rad}} + h_{\text{air}})S_s(T_c - T_0) \simeq 0.6$ mW for a FSR having a radius $R_s = 0.1$ mm. In the region where SBs are observed the induced heating power applied to the FSR is about three orders of magnitudes larger, hence $H \simeq H_{\text{fer}}$, i.e., both radiation and air have negligibly small contributions, and thus heat is mainly removed by the ferrules.

The thermal heat capacity of a FSR having a radius $R_s = 0.1$ mm and volume $V_s = 4\pi R_s^3/3$ is given by $C = 2.9 \times 10^6$ $\text{J K}^{-1} \text{m}^{-3} \times V_s = 1.2 \times 10^{-5}$ J K^{-1} [51], hence the thermal decay rate is roughly given by $H/C \simeq 320$ $\text{Hz} \times (Q_c/W)[(T_c - T_0)/(260 \text{ K})]^{-1}$, where Q_c is the heating power

applied to the FSR, for which the steady state temperature is T_c . Hence for the current device, $(H/C)/\gamma_+ \simeq 10^{-5}$, and thus the diabatic approximation is applicable.

A typical limit cycle (LC) in the diabatic regime is shown in Fig. 4. The LC is calculated by numerically integrating the equations of motion (4) and (5). The blue (red) cross shown in Fig. 4(a) indicates the steady state value w_1/w of B corresponding to the FS (PS), i.e., for $\Theta < 1$ ($\Theta > 1$), and the blue (red) circle represents the relation $|B|^2 = E_{cF}$ ($|B|^2 = E_{cP}$). In the plane of driving frequency and driving amplitude, which is shown in Fig. 4(b), the blue and red curves are derived from the relations $E_F = E_{cF}$ and $E_P = E_{cP}$, respectively. In the region labeled as A, no steady state solution to Eqs. (4) and (5) exists. The LC period time τ_{LC} can be calculated by integrating Eqs. (4) and (5) over a single period. In the diabatic limit, one finds that $\tau_P \simeq |w_P|^{-1} + |w_F|^{-1}$. The measured value of LC frequency roughly agrees with this theoretical estimation.

V. SUMMARY

In summary, we demonstrate that a relatively large coupling coefficient g_{eff} can be obtained by employing an LGR having a mode volume much smaller than λ_c^3 . The response of the system in the weak nonlinear regime allows the extraction of the Kerr coefficient K_M and the cubic nonlinear damping rate γ_{3s} . An instability is revealed by driving the system with a relatively high input power. Above the instability threshold the response of the system to an externally applied monochromatic driving exhibits self-modulation. The instability, which is attributed to driving-induced heating, occurs in a region where the response has no steady state value. Further study will be devoted to developing sensors that exploit this instability for performance enhancement.

ACKNOWLEDGMENTS

This work was supported by the Israeli Science Foundation Grant No. 963/19, the Israeli Ministry of Science, and by the Technion Security Research Foundation.

APPENDIX: ROTATING WAVE APPROXIMATION

The Hamiltonian (1) can be expressed as

$$\hbar^{-1}\mathcal{H}_D = (A_e^\dagger \quad A_s^\dagger)M \begin{pmatrix} A_e \\ A_s \end{pmatrix} + K_M N_s^2, \quad (\text{A1})$$

where the 2×2 matrix M is given by

$$M = \begin{pmatrix} \omega_e & g_{\text{eff}} \\ g_{\text{eff}} & \omega_s \end{pmatrix}. \quad (\text{A2})$$

The eigenvalues ω_\pm of the matrix M are given by $\omega_\pm = \omega_m \pm \sqrt{\omega_d^2 + g_{\text{eff}}^2}$ [see Eq. (2)], where $\omega_m = (\omega_e + \omega_s)/2$ and $\omega_d = (\omega_e - \omega_s)/2$. The matrix M can be expressed as

$$M = \omega_m \begin{pmatrix} 1 & 0 \\ 0 & 1 \end{pmatrix} + \sqrt{\omega_d^2 + g_{\text{eff}}^2} \begin{pmatrix} \cos \theta & \sin \theta \\ \sin \theta & -\cos \theta \end{pmatrix}, \quad (\text{A3})$$

where

$$\tan \theta = \frac{g_{\text{eff}}}{\omega_d}. \quad (\text{A4})$$

The transformation

$$\begin{pmatrix} A_e \\ A_s \end{pmatrix} = U \begin{pmatrix} A_+ \\ A_- \end{pmatrix}, \quad (\text{A5})$$

where

$$U = \begin{pmatrix} \cos \frac{\theta}{2} & -\sin \frac{\theta}{2} \\ \sin \frac{\theta}{2} & \cos \frac{\theta}{2} \end{pmatrix}, \quad (\text{A6})$$

which diagonalizes the linear part of \mathcal{H}_D , yields

$$\hbar^{-1}\mathcal{H}_D = \omega_+ N_+ + \omega_- N_- + K_M (A_s^\dagger A_s)^2, \quad (\text{A7})$$

where $A_s = A_+ \sin(\theta/2) + A_- \cos(\theta/2)$, and where $N_\pm = A_\pm^\dagger A_\pm$.

In the rotating wave approximation (RWA) the Hamiltonian (A7) becomes

$$\begin{aligned} \hbar^{-1}\mathcal{H}_D = & \omega_+ N_+ + \omega_- N_- \\ & + K_+ N_+^2 + K_- N_-^2 + K_i N_+ N_-, \end{aligned} \quad (\text{A8})$$

where the Kerr coefficients K_\pm are given by

$$K_+ = \bar{K}_M \sin^4 \frac{\theta}{2}, \quad (\text{A9})$$

$$K_- = K_M \cos^4 \frac{\theta}{2}, \quad (\text{A10})$$

and the intermode Kerr coefficient K_i is given by $K_i = K_M \sin^2 \theta$.

-
- [1] R. M. Hill and R. S. Bergman, *J. Appl. Phys.* **32**, S227 (1961).
 [2] R. LeCraw, E. Spencer, and C. Porter, *Phys. Rev.* **110**, 1311 (1958).
 [3] R. Kumar, B. Samantaray, and Z. Hossain, *J. Phys.: Condens. Matter* **31**, 435802 (2019).
 [4] M. Rytel, P. Kopyt, and B. Salski, in *2018 22nd International Microwave and Radar Conference (MIKON)* (IEEE, Piscataway, NJ, 2018), pp. 434–437.
 [5] C. Tsai, G. Qiu, H. Gao, L. Yang, G. Li, S. Nikitov, and Y. Gulyaev, *IEEE Trans. Magn.* **41**, 3568 (2005).
 [6] K. Kotzebue and L. Fletcher, *IEEE Trans. Microwave Theory Tech.* **13**, 773 (1965).
 [7] S. M. Rezende, *Fundamentals of Magnonics*, Lecture Notes in Physics Vol. 969 (Springer, Berlin, 2020).
 [8] S. Demokritov, V. Demidov, O. Dzyapko, G. Melkov, A. Serga, B. Hillebrands, and A. Slavin, *Nature (London)* **443**, 430 (2006).
 [9] X. Zhang, N. Zhu, C.-L. Zou, and H. X. Tang, *Phys. Rev. Lett.* **117**, 123605 (2016).
 [10] A. Osada, R. Hisatomi, A. Noguchi, Y. Tabuchi, R. Yamazaki, K. Usami, M. Sadgrove, R. Yalla, M. Nomura, and Y. Nakamura, *Phys. Rev. Lett.* **116**, 223601 (2016).
 [11] D. D. Stancil and A. Prabhakar, *Spin Waves* (Springer, Berlin, 2009).

- [12] Y. Kajiwara, K. Harii, S. Takahashi, J.-i. Ohe, K. Uchida, M. Mizuguchi, H. Umezawa, H. Kawai, K. Ando, K. Takanashi *et al.*, *Nature (London)* **464**, 262 (2010).
- [13] V. Cherepanov, I. Kolokolov, and V. L'vov, *Phys. Rep.* **229**, 81 (1993).
- [14] A. Serga, A. Chumak, and B. Hillebrands, *J. Phys. D: Appl. Phys.* **43**, 264002 (2010).
- [15] S. Rezende, F. De Aguiar, and O. de Alcantara Bonfim, *J. Magn. Magn. Mater.* **54**, 1127 (1986).
- [16] S. M. Rezende and F. M. de Aguiar, *Proc. IEEE* **78**, 893 (1990).
- [17] S. Sharma, Y. M. Blanter, and G. E. W. Bauer, *Phys. Rev. Lett.* **121**, 087205 (2018).
- [18] R. Jepsen, *J. Appl. Phys.* **32**, 2627 (1961).
- [19] F. R. Morgenthaler, *J. Appl. Phys.* **30**, S157 (1959).
- [20] Y.-P. Wang, G.-Q. Zhang, D. Zhang, T.-F. Li, C.-M. Hu, and J. Q. You, *Phys. Rev. Lett.* **120**, 057202 (2018).
- [21] Y.-P. Wang, G.-Q. Zhang, D. Zhang, X.-Q. Luo, W. Xiong, S.-P. Wang, T.-F. Li, C.-M. Hu, and J. Q. You, *Phys. Rev. B* **94**, 224410 (2016).
- [22] P. Hyde, B. M. Yao, Y. Gui, G.-Q. Zhang, J. Q. You, and C.-M. Hu, *Phys. Rev. B* **98**, 174423 (2018).
- [23] H. Suhl, *J. Phys. Chem. Solids* **1**, 209 (1957).
- [24] G. Wiese and H. Benner, *Z. Phys. B: Condens. Matter* **79**, 119 (1990).
- [25] M. G. Cottam and Z. Haghshenasfard, *Phys. Canada* **72**, 63 (2016).
- [26] M. Elyasi, Y. M. Blanter, and G. E. W. Bauer, *Phys. Rev. B* **101**, 054402 (2020).
- [27] Z. Zhang, M. O. Scully, and G. S. Agarwal, *Phys. Rev. Research* **1**, 023021 (2019).
- [28] X. Zhang, C.-L. Zou, L. Jiang, and H. X. Tang, *Phys. Rev. Lett.* **113**, 156401 (2014).
- [29] Y. Tabuchi, S. Ishino, T. Ishikawa, R. Yamazaki, K. Usami, and Y. Nakamura, *Phys. Rev. Lett.* **113**, 083603 (2014).
- [30] D. Lachance-Quirion, Y. Tabuchi, A. Gloppe, K. Usami, and Y. Nakamura, *Appl. Phys. Express* **12**, 070101 (2019).
- [31] D. Lachance-Quirion, S. P. Wolski, Y. Tabuchi, S. Kono, K. Usami, and Y. Nakamura, *Science* **367**, 425 (2020).
- [32] Y. Tabuchi, S. Ishino, A. Noguchi, T. Ishikawa, R. Yamazaki, K. Usami, and Y. Nakamura, *C. R. Phys.* **17**, 729 (2016).
- [33] S. V. Kusminskiy, *arXiv:1911.11104*.
- [34] R. Denton, *J. Appl. Phys.* **32**, S300 (1961).
- [35] X. Zhang, C.-L. Zou, L. Jiang, and H. X. Tang, *Sci. Adv.* **2**, e1501286 (2016).
- [36] J. C. Slonczewski, *J. Magn. Magn. Mater.* **159**, L1 (1996).
- [37] S. I. Kiselev, J. Sankey, I. Krivorotov, N. Emley, R. Schoelkopf, R. Buhrman, and D. Ralph, *Nature (London)* **425**, 380 (2003).
- [38] C. Safranski, I. Barsukov, H. K. Lee, T. Schneider, A. Jara, A. Smith, H. Chang, K. Lenz, J. Lindner, Y. Tserkovnyak *et al.*, *Nat. Commun.* **8**, 117 (2017).
- [39] S. Daimon, R. Iguchi, T. Hioki, E. Saitoh, and K.-i. Uchida, *Nat. Commun.* **7**, 13754 (2016).
- [40] G. Zhang, Y. Wang, and J. You, *Sci. China: Phys., Mech. Astron.* **62**, 987511 (2019).
- [41] T. Holstein and H. Primakoff, *Phys. Rev.* **58**, 1098 (1940).
- [42] C. Mathai, S. Masis, O. Shtempluck, S. Hacothen-Gourgy, and E. Buks, *Europhys. Lett.* **131**, 67001 (2020).
- [43] L. Sainz de los Terreros and F. J. Bermejo, *Phys. Rev. A* **45**, 1906 (1992).
- [44] P. Kirton, M. M. Roses, J. Keeling, and E. G. Dalla Torre, *Adv. Quantum Technol.* **2**, 1800043 (2019).
- [45] M. R. Jeffrey, A. R. Champneys, M. di Bernardo, and S. W. Shaw, *Phys. Rev. E* **81**, 016213 (2010).
- [46] W. Froncisz and J. S. Hyde, *J. Magn. Reson. (1969)* **47**, 515 (1982).
- [47] D. Zhang, W. Song, and G. Chai, *J. Phys. D: Appl. Phys.* **50**, 205003 (2017).
- [48] J. Krupka, K. Derzakowski, M. Tobar, J. Hartnett, and R. G. Geyer, *Meas. Sci. Technol.* **10**, 387 (1999).
- [49] B. Yurke and E. Buks, *J. Lightwave Technol.* **24**, 5054 (2006).
- [50] D. Wood and J. Remeika, *J. Appl. Phys.* **38**, 1038 (1967).
- [51] A. M. Hofmeister, *Phys. Chem. Miner.* **33**, 45 (2006).